Available online at www.sciencedirect.com

ScienceDirect

Journal of Nuclear Materials 371 (2007) 145–160

journal of nuclear materials

www.elsevier.com/locate/jnucmat

Embrittlement of RPV steels: An atom probe tomography perspective

M.K. Miller *, K.F. Russell

Microscopy Group, Materials Science and Technology Division, Oak Ridge National Laboratory, P.O. Box 2008,
Building 4500S, MS 6136, Oak Ridge, TN 37831-6136, USA

Abstract

Atom probe tomography has played a key role in the understanding of the embrittlement of neutron irradiated reactor pressure vessel steels through the atomic level characterization of the microstructure. Atom probe tomography has been used to demonstrate the importance of the post weld stress relief treatment in reducing the matrix copper content in high copper alloys, the formation of ~2-nm-diameter copper-, nickel-, manganese- and silicon-enriched precipitates during neutron irradiation in copper containing RPV steels, and the coarsening of these precipitates during post irradiation heat treatments. Atom probe tomography has been used to detect ~2-nm-diameter nickel-, silicon- and manganese-enriched clusters in neutron irradiated low copper and copper free alloys. Atom probe tomography has also been used to quantify solute segregation to, and precipitation on, dislocations and grain boundaries.
Published by Elsevier B.V.

1. Introduction

The characterization of the fine scale microstructural features responsible for the embrittlement of reactor pressure vessel (RPV) steels and related alloys after exposure to neutron irradiation has been the focus of many experimental studies. Two complementary techniques, atom probe tomography (APT) and small angle neutron scattering (SANS), have emerged as powerful experimental techniques for the characterization of these neutron irradiated materials due to the fine scale of the microstructural features responsible for the embrittlement.

Several different types of RPV materials have been investigated by APT including plate, forgings, and welds from commercial Western and Russian variants of pressure vessels, test reactor irradiated steels, and model alloys with systematic alloying additions. These materials have been characterized in the irradiated, irradiated and annealed conditions and also after long term thermal aging. In this paper, a brief outline of atom probe tomography and its application to the characterization of RPV steels is presented.

2. Atom probe tomography

Since the first characterizations of a neutron irradiated Fe–0.34% Cu binary alloy by field ion microscopy in 1978 [1] and a neutron irradiated

---

* Corresponding author. Tel.: +1 865 574 4719; fax: +1 865 241 3650.
E-mail address: millermk@ornl.gov (M.K. Miller).

0022-3115/$ - see front matter Published by Elsevier B.V.
doi:10.1016/j.jnucmat.2007.05.003

RPV steel by atom probe field ion microscopy in 1979 that conclusively proved the existence of ~2-nm-diameter copper-enriched precipitates [2,3], many major advances have been made to the instruments and the methodologies for the quantification of the data. The first type of atom probe used in these studies featured an ~1-mm-diameter aperture that defined the entrance to the time-of-flight mass spectrometer [4]. Due to the million times magnification of the instrument, this circular aperture defined an ~1-nm-diameter region on the specimen surface. Therefore as the sample was field evaporated, the atoms in a cylindrical volume of material defined by the aperture were collected in the time-of-flight spectrometer. In this atom probe field ion microscope, atoms were collected from significantly less than 1% of the specimen. Reviews of the characterizations performed on irradiated RPV steels with these early types of atom probe were reported in 1989 [5,6]. Approximately a decade later, the introduction of a new generation of three-dimensional atom probes (3DAP) featuring position-sensitive, single atom sensitive detectors noticeably improved the extent of the volume analyzed to a region 10–20 nm in diameter or 10–20 nm on each side of a square [6,7]. These instruments enabled volumes containing between ~100 000 and a million atoms to be collected. These experiments took many hours due to the 50–2000 Hz repetition rate of the high voltage pulse generator used to field evaporate the individual atoms from the specimen. Some reviews of the characterization performed with these 3DAPs have been reported [8–11]. More recently, the commercial availability of the local electrode atom probe (LEAP®) has again significantly increased the field of view to over 50 by 50 nm and also dramatically reduced the time required to perform the experiments due to its 200 kHz pulse generator. A schematic diagram of this instrument is shown in Fig. 1. With this instrument under appropriate experimental conditions for full quantitative analysis, volumes containing up to 100 million atoms can be reliably collected at rates of approximately a million atoms every 5 min. Due to the brittleness of neutron irradiated RPV steels (and the fracture of the atom probe specimen under the high stress applied during analysis), typical analyzed volumes contain between 1 and 20 million atoms. Because of the use of microchannel plates in the position-sensitive single atom sensitive detector, Fig. 1, the detection efficiency of the time-of-flight mass spectrometer in all these variants is typically 50–60%. The atom probe is equally sensitive to and is able to detect all elements. The mass resolving power of the atom probe is sufficient to resolve the individual isotopes of the elements. Solute concentrations are estimated from counting the number of atoms of each element in the volume of analysis, as discussed below. Ongoing developments in atom probe position-sensitive detector designs should further increase the field of view and the re-introduction of laser-assisted field evaporation should enable more brittle materials to be routinely characterized.

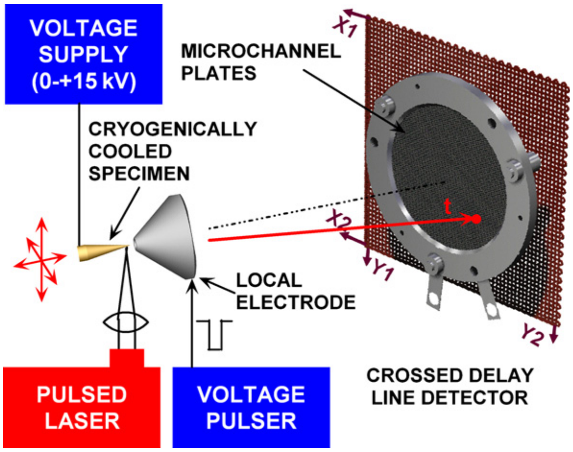

Fig. 1. Schematic diagram of a local electrode atom probe showing the needle-shaped specimen mounted on a 3-axis stage, the field defining local electrode and the position-sensitive single atom cross delay line detector. Atoms may be field evaporated from the specimen with either the voltage pulse generator or the pulsed laser.

Sample preparation of irradiated steels is performed in a hot cell environment. The bulk material is initial cut into 0.25 × 0.25 × ~10 mm blanks. Because of the mass of this small volume, each blank generally has low activity. This blank is electropolished into the required needle-shaped atom probe specimen geometry with an apex radius of ~50 nm [4,6,7]. After electropolishing, the activity is reduced further. The same specimen can often be repolished several times to further reduce the volume of material. However, safety procedures for the handling of radioactive materials are required to examine these steels in the atom probe.

3. Data processing

In addition to the instrument developments, significant advances have been made in the visualization and analysis of the data collected [7]. The basic data generated in atom probe tomography are the atomic coordinates and mass-to-charge state ratio of each atom in the volume analyzed [7]. These data can be processed in a variety of ways. The most common visualization method is the atom map, as shown in Fig. 2 for a neutron irradiated pressure vessel steel weld. In these atom maps, a small color-coded sphere is used to indicate the position of each atom. The atoms of the major element, i.e., iron, are not shown for clarity. A copper-, manganese-, nickel-, and silicon-enriched precipitate is clearly visible in this selected volume. Due to slight differences in local magnification between the precipitate and the matrix, solute enrichments should not be inferred from the atom density in these maps but from concentration estimates. The number density is estimated from the number of precipitates, n_p, in the volume, where the volume, v, is estimated from the total number of atoms, n, and the atomic volume, Ω, of the appropriate crystal structure (i.e., body centered cubic (bcc) Fe) and a calibrated detection efficiency, ξ, i.e., $N_v = n_p/v = n_p\xi/n\Omega$. In the local electrode atom probe, precipitates with number densities greater than $\sim 10^{22}\ \mathrm{m^{-3}}$ may be detected and their parameters quantified.

Due to the small size and the small number of atoms in these copper-enriched precipitates, the estimation of their size and composition requires some careful consideration as to which atoms belong to the matrix and which are associated with the precipitate. For example, 1-, 2- and 4-nm-diameter bcc precipitates, with a lattice parameter of $a_0 = 0.288$ nm, typically contain only 55, 350 and 2800 atoms, respectively. A simulation of typical 2-nm-diameter spherical precipitates with a number density of $1 \times 10^{24}\ \mathrm{m^{-3}}$ is shown in Fig. 3. The atoms in each precipitate, ∼350, and its facetted surface are shown in Fig. 3(a). Note that some precipitates are cut by the 10 × 10 × 10 nm bounding box. As the detection efficiency of the atom probe is typically 50–60%, not all these atoms are detected, as shown in Fig. 3(b). Additionally, small aberrations in the

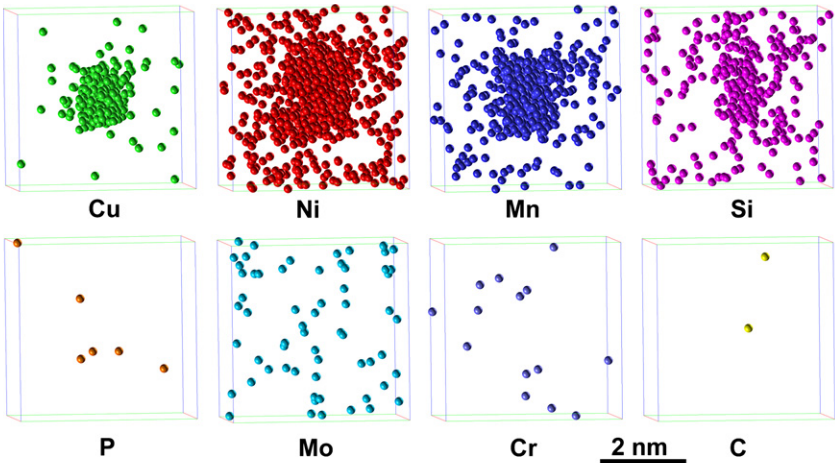

Fig. 2. Atom maps of a copper-, nickel-, manganese- and silicon-enriched precipitate in a model pressure vessel steel neutron irradiated to a fluence of $1.6 \times 10^{23}\ \mathrm{m^{-2}}$ ($E > 1$ MeV).

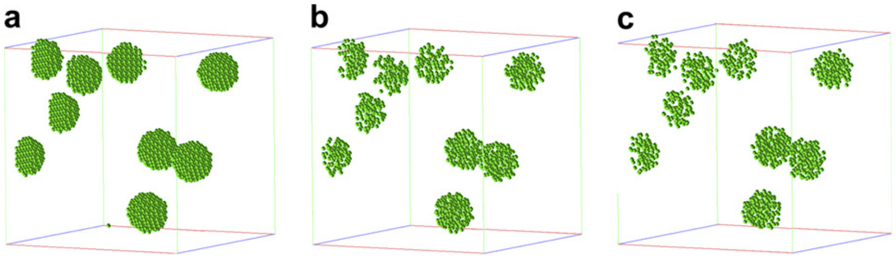

Fig. 3. Atom simulations of 2-nm-diameter precipitates with 100% solute. (a) All atoms with 100% detection efficiency, (b) 50% detection efficiency and (c) 50% detection efficiency with a position scatter of 0.2 nm.

trajectory of the ions occur as they leave the specimen thereby moving the atoms off their lattice positions in the reconstruction, as shown in Fig. 3(c).

The solute concentration of element a, C_a, in a precipitate or the matrix is determined by counting the number of atoms of each element, n_a, i.e., $C_a = n_a/n_T$ within a sampled volume of that feature, where n_T is the total number of atoms in the sampled volume. The standard deviation of this measurement is given by $\sigma = \sqrt{(C_a(1 - C_a))/n_T}$. As the smallest precipitates contain very few atoms, counting statistics are important in the composition determination and a difference of only one or two solute or solvent atoms has a significant effect on the estimated solute concentration. In addition, the small number of atoms in the precipitate limits the minimum measurable solute concentration for an individual precipitate. A more important issue is the exact definition of the precise location of the precipitate–matrix interface and the contribution of the solvent atoms, i.e., iron, on the surface of the precipitate, particularly when the precipitate contains some solvent atoms. In the 1–2 nm size range, the majority of the atoms are in the surface layer of the precipitate. Therefore, some definition must be used to determine whether a solvent atom on the surface of the precipitate belongs to the precipitate or the matrix. If all solvent atoms on the surface are assigned to the matrix, the solute concentration of the precipitate will be overestimated. Conversely if these atoms are assigned to the precipitate, the solute concentration will be underestimated. Unfortunately, there is no definitive answer to this question, which has resulted in some confusion as to the composition of these precipitates estimated by different atom probe groups and when comparing the atom probe estimates to those obtained from other techniques such as small angle neutron scattering. This issue is complicated further when there are solute gradients of the primary solute atoms, e.g., copper, and gradients or interfacial segregation of other elements, such as nickel, manganese and silicon, as shown in the atom maps in Fig. 2.

Hyde developed a maximum separation method [12] to estimate the size of these precipitates that is based on a friend-of-friends concept. The method is based on the concept that the solute in a solute-enriched precipitate are closer together than the solute atoms in a dilute solid solution. Therefore, the solute atoms in the precipitate can be identified as the solute atoms that are within a maximum separation distance, d_{max}, from one another. This method detects solute agglomerations containing 2 or more atoms of interest. However, some of the smaller agglomerations are expected from the solute distribution in a random solid solution. Therefore, a minimum size cutoff limit, n_{min}, is used to eliminate these agglomerations. The value used for the cutoff is estimated either from the analyses of APT data from a solid solution or from a simulation of random solid solution with the same parameters as the alloy under investigation including the matrix solute level, atomic density (i.e., crystal structure and lattice parameters), and detection efficiency [13,14]. The estimate of the cutoff limit is an upper limit; when phase separation or precipitation occurs, the solute level in the matrix decreases, resulting in an increase in the separation of similar atoms in the matrix. Once all the solute atoms in the precipitates are identified, its size can be estimated from the positions of these atoms by a standard radius of gyration, l_g, equation [7]. The Guinier radius for spherical precipitates is given by $r_G = 1.29 l_g$. The algorithm is most effective when the matrix solute level is low and there is a substantial solute content in the precipitate, which is the case for the copper-enriched precipitates found in neutron irradiated RPV steels. At matrix concentrations above $\approx 1\%$, the solute atoms become too close together to distinguish matrix and precipitate solute atoms and the algorithm is not appropriate. New methods are under development for these cases.

These methods can also be applied to estimate the extent and level of solute segregation to dislocations. In order to estimate the extent of the segregation, a volume surrounding the dislocation is selected such that the line of the dislocation is parallel to the major axis of the volume. The maximum separation method is applied to identify the solute atoms associated with the dislocation. The extent of the segregation is estimated from the two radii of gyrations in the directions perpendicular to the selected major axis.

Several methods have been used to estimate the composition of precipitates from atom probe data. In the envelope extension to the maximum separation method [7], a fine three-dimensional grid of volume elements (or voxels) is superimposed on the data. The selected solute atoms identified by the maximum separation method that belong to the precipitates are then used to identify the voxels belonging to each precipitate. Due to the fine scale of the grid, typically less than 0.2 nm, some voxels in the interior of the precipitate may not contain any of the selected solute atoms but are included in the composition estimate if they are surrounded by voxels that contain selected solute atoms. The solute concentrations are then determined by counting the number of atoms of each element within this three-dimensional envelope. An alternative recursive search algorithm that assigns atoms to the matrix or the precipitate based on their local environment may also be used [12]. This algorithm is less aggressive in removing the solvent atoms.

The solute profile and interfacial segregation behavior may also be characterized in the ultrafine precipitates. One method is to calculate spherical shells from the center of mass of the precipitate. The center of mass is calculated from the position of the selected solute atoms found by the maximum separation method. However, this method is only applicable to spherical precipitates. Linear concentration profiles have also been used in which a rectangular or cylindrical volume is selected that passes through the precipitate. However, this method generally suffers from simultaneous sampling of the matrix and the precipitate and results in averaging of the concentration estimates or has large error bars on the concentration estimates due to the small sample size. Another method is to create an isoconcentration interface with a marching cube algorithm and then count the atoms within thin volume slices parallel to this surface. This method is applicable to precipitates (and interfaces) with any morphology and is known as a proximity histogram or proxigram [15]. A comparison of a radial concentration profile and a proxigram to the copper-enriched precipitates in an irradiated pressure vessel steel is shown in Fig. 4. The methods may be applied to individual precipitates or may be averaged over several precipitates to reduce the statistical scatter due to the small number of atoms in each precipitate. Good agreement between the two methods is evident in Fig. 4. In this typical example, the extents of the nickel, manganese and silicon atoms are slightly larger than that of copper, indicating interfacial segregation of these elements. The levels of nickel and manganese in the interior of the precipitate were higher than the matrix level indicating solute partitioning.

4. Microstructure

Many factors including alloy type and composition, prior heat treatment history, irradiation temperature, neutron fluence and flux, etc. influence the microstructure and consequently the susceptibility of the steel to embrittlement during neutron irradiation. RPV steels have complex ferritic, tempered martensitic, or bainitic microstructures that contain distributions of 10 nm to micrometer size precipitates, including cementite (Fe_3C), Mo_2C, $M_{23}C_6$, M_7C_3, V(CN), etc. depending on the type of steel. These coarse precipitates do not change significantly during service in the nuclear reactor. As some of the alloying elements preferentially partition to these precipitates and therefore deplete the matrix of these solutes, their compositions, sizes and volume fractions are an important component in fully understanding the solute partitioning between the microstructural features. Due to their low volume fraction, coarse precipitates are only occasionally encountered in atom probe analyses. In addition, the high evaporation field and poor electrical conductivity of refractory carbides have made their

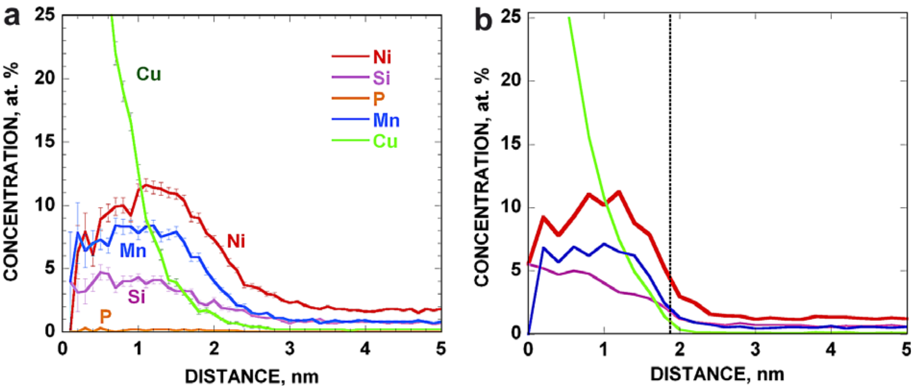

Fig. 4. (a) Averaged radial concentration profile from the center of masses of 30 copper-enriched precipitates and (b) corresponding proximity histogram. Vertical dashed line in (b) is the position of the master isoconcentration surface.

characterizations in the atom probe challenging. The recent re-introduction of laser-assisted field evaporation and new wider field-of-view atom probes coupled with focused ion beam based specimen preparation techniques will enable these types of precipitates to be more readily analyzed. Some examples of the compositions of these precipitates have been reported in previous atom probe studies [5].

The atomic scale microstructural features that are commonly found in neutron irradiated pressure vessel steels are described in the following sections. Many different forgings, plates and welds from both Western and VVER type reactors have been characterized by atom probe tomography. The development of fine scale microstructural features depends more on the precise composition of the steel rather than the base microstructure. These commercial RPV steels have encompassed a relatively narrow range of compositions. In order to fully understand the roles of individual alloying elements, model alloys with systematic variations in the alloying additions have also been studied, and the atom probe results of these model alloys will be reported in detail elsewhere.

5. Importance of the post weld or stress relief heat treatment

One of the most important steps of the heat treatment history for high copper alloys is the stress relief treatment and subsequent cooling rate to room temperature [16]. The stress relief treatment is typically performed in the 600–620 °C temperature range for several hours. Consequently in high copper alloys, the matrix copper level will be reduced to the copper solubility level at that temperature through the precipitation of ε-copper precipitates at grain boundaries [5] and on dislocations. Some additional reduction in the copper level will also occur during the cool to room temperature due to the high heat capacity of the thick sections used in reactor vessels. It has been experimentally demonstrated from atom probe and thermoelectric power (TEP) data [17] that simple extrapolation of high temperature binary Fe–Cu solubility data and thermodynamic predictions do not yield reliable values at either these stress relief or lower reactor operating temperatures due to kinetic effects and the influence of other solute elements. Atom probe experiments revealed that the matrix copper level of the weld in the Midland reactor was reduced from 0.18–0.28 at.% Cu to 0.12 ± 0.01 at.% Cu after a stress relief treatment of 22.5 h at 607 °C [18]. In a high copper weld, designated 73 W, lower stress relief temperatures and slower cooling rates have been shown to lower the matrix copper level [19]. This lower matrix copper content is beneficial as the reduced supersaturation should result in a lower number density of copper-enriched precipitates being formed during neutron irradiation. However, the lower temperature may be detrimental for other temperature sensitive segregation processes [20]. The maximum matrix copper level also is an important parameter to consider when high copper model alloys are used to simulate trends in actual RPV steels.

6. Intragranular precipitation and solute clustering

Apart from the coarse carbides and precipitates formed during the post welding stress relief treatment and some dislocations, the matrices of unirradiated RPV steels are generally found to be solid solutions with no fine scale precipitates or solute clustering.

Fine scale precipitates are not typically observed in neutron irradiated welds, forgings and plates with copper contents below ~0.05 at.% Cu or nickel levels below ~1.2% Ni. In steels with higher copper levels, high number densities of ultrafine copper-enriched precipitates are observed, as shown in Fig. 2. A set of atom maps for all solute elements in the radiation sensitive high copper (0.37 wt% Cu) high nickel (1.23 wt% Ni), high manganese (1.64 wt% Mn) KS-01 weld that was neutron irradiated to a relatively low fluence of 0.8×10^{23} n m^{-2} ($E > 1$ MeV) at a temperature of 288 °C is shown in Fig. 5. This weld exhibited a large Charpy $T_{41\,\mathrm{J}}$ shift of 169 K and a significant decrease in upper-shelf energy (USE) from 118 J to ~78 J [21,22]. A high number density (~3×10^{24} m^{-3}) of copper-, manganese-, nickel-, silicon and phosphorus-enriched precipitates, with an average radius of gyration of 3.3 ± 0.6 nm, is evident.

A typical size distribution of similar copper-enriched precipitates in a high-copper (0.20 wt% Cu), high-nickel (1.20 wt%) weld from the Palisades reactor [23] that was irradiated in the Ford reactor at a temperature of 288 °C and a flux of ~7×10^{11} cm^{-2} s^{-1} to a fast fluence of 3.4×10^{23} n m^{-2} ($E > 1$ MeV) is shown in Fig. 6. The average radius of gyration of 235 precipitates from this and a second local electrode atom probe analysis was

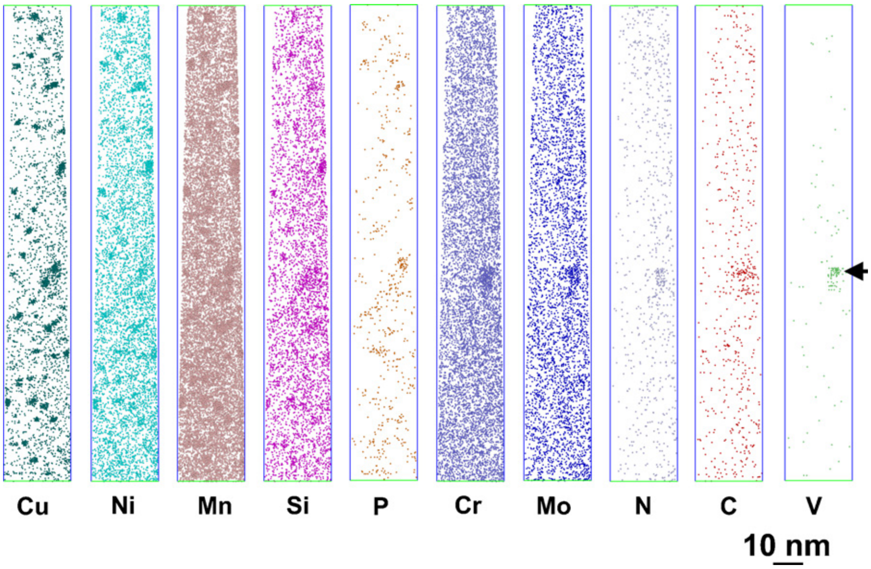

Fig. 5. Atom maps from a KS-01 weld that was neutron irradiated to a fluence of 0.8×10^{23} n m^{-2} ($E > 1$ MeV) at a temperature of 288 °C. A high number density ($\sim 3 \times 10^{24}$ m^{-3}) of Cu-, Mn-, Ni-, Si- and P-enriched precipitates with an average radius of gyration of 3.3 ± 0.6 nm is evident. A Cr-, Mn-, Ni-, Cu-, C-, N-, Si- and Mo-enriched feature (arrowed) is also evident.

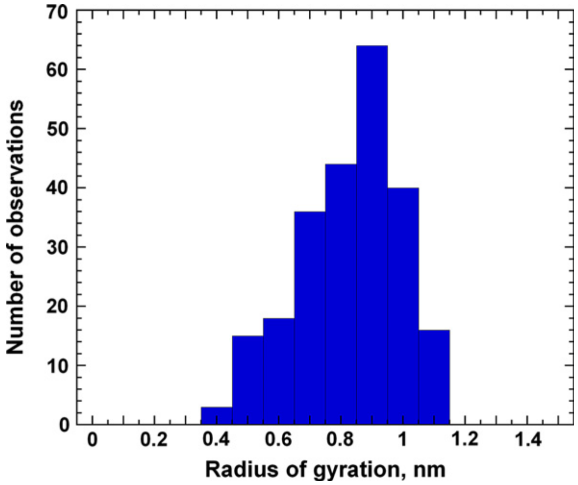

Fig. 6. Size distribution of copper-enriched precipitates in the neutron irradiated weld from the Palisades reactor.

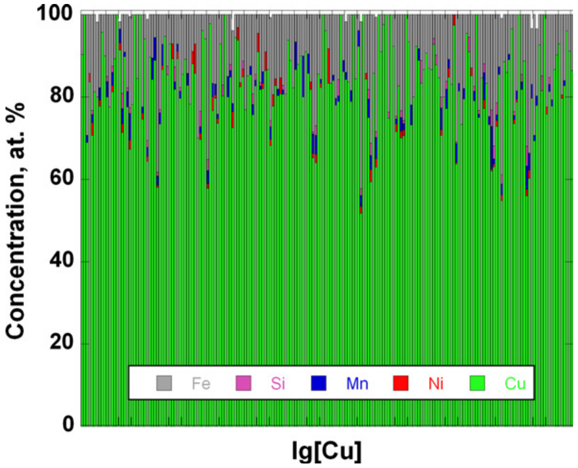

Fig. 7. The compositions of copper-enriched precipitates from the neutron irradiated weld from the Palisades reactor.

estimated to be 0.82 ± 0.16 nm. This yields an average Guinier radius of 1.0 ± 0.2 nm. The number density was estimated to be $\sim 5 \times 10^{23}$ m^{-3}. The compositions of the core of these precipitates, as estimated from the maximum separation envelope method with a maximum separation distance of 0.6 nm and a grid size of 0.1 nm, are shown schematically in Fig. 7. In this figure, the precipitate compositions have been sorted by size with size increasing from left to right. No significant variation of the composition with size was observed. The white bars on some of the measurements indicate the presence of the other alloying elements in the steel. The average composition of the core of these precipitates was estimated by the envelope method to be Fe–83 ± 10 at.% Cu, 2.3% Ni, 1.5% Mn, 0.5% Si.

Some phosphorus enrichment has also been observed in these precipitates particularly in high phosphorous (0.017 wt%, 0.031 at.% P) alloys such

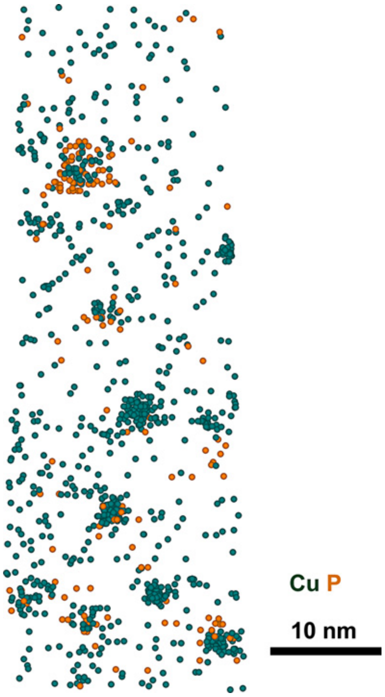

Fig. 8. Atom map from the KS-01 weld that was neutron irradiated to a fluence of 0.8×10^{23} n m^{-2} ($E > 1$ MeV) at a temperature of 288 °C showing phosphorus segregation to the copper-enriched precipitates and a phosphorus cluster.

as the KS-01 weld, as shown in the atom map in Fig. 8. The average radius of gyration of the P clusters was estimated to be 5.6 ± 3.3 nm and their average composition was estimated by the envelope method to be Fe–54 ± 12% P, 1.6 ± 1.6% Mn, 1 ± 1% Ni, 0.5 ± 0.5% Cu and 0.5 ± 0.5% Mo.

The crystal structure of these copper-enriched precipitates has not been confirmed as the other standard high resolution transmission electron microscopy, X-ray diffraction and other techniques are unable to resolve them at their earliest stage of formation. The matching of crystallographic planes of these precipitates and the surrounding body centered cubic (bcc) matrix in both field ion images and atom maps [24] suggests that these precipitates have a bcc crystal structure and are therefore a precursor to the equilibrium face centered cubic ε-Cu precipitate.

Although the term precipitate is used here to describe the ultrafine copper-enriched regions, several other terms such as clusters, nanoclusters, embryos, or atmospheres can also be used. It may also be correct to describe the initial regions as Guinier-Preston zones. It should not be inferred from this precipitate terminology that these features are thermodynamically stable or at equilibrium.

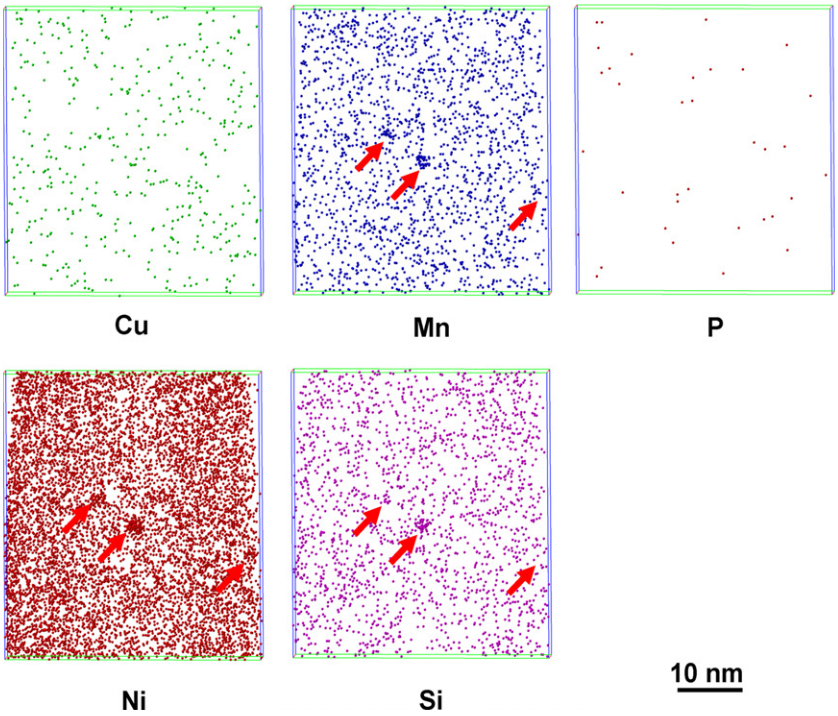

Fig. 9. Ultrafine Mn-, Ni- and Si-enriched clusters in a neutron irradiated fluence 2.4×10^{23} n m^{-2} ($E > 0.5$ MeV) low copper (0.05% Cu) weld from a VVER1000 reactor.

Another form of solute clustering has been observed in low copper and copper-free alloys that also have high nickel contents. An example of these nickel-, manganese- and silicon-enriched clusters in a weld with a Russian VVER 1000 type reactor composition that was neutron irradiated in the Ford test reactor to a total fluence of 1.4×10^{23} n m^{-2} (>1 MeV) [2.4×10^{23} n m^{-2} (>0.5 MeV)] at a temperature of 288 °C is shown in Fig. 9 [25]. These ~1–2-nm-diameter clusters are similar in size to or slightly smaller than the copper-enriched precipitates. As these clusters were originally thought to only form after exposure to high fluences and were therefore termed 'late-blooming phases' [26], they are a concern for plant life extension especially in low copper, high nickel welds. Research to establish the parameter space for the formation of these clusters is ongoing. One possibility is that the clusters form due to phase separation in a low temperature miscibility gap. The phase separation may have a long incubation time at this low temperature or it may be due to a spinodal-type reaction. The shorter incubation time copper-enriched precipitates may also form a nucleus onto which these clusters can nucleate and grow and hence appear as the observed nickel-, manganese- and silicon-enriched shell. This phase separation/cluster formation may also be related to the nickel and silicon segregation to dislocations.

7. Dislocations

The atom probe is unique in that it can detect and quantify solute segregation and precipitation on individual dislocations [27–29]. Many examples of phosphorus segregation to dislocations have been observed in atom probe studies of RPV steels. An example of phosphorus segregation to a dislocation in a weld from the Midland reactor after exposure to a fluence of 1.1×10^{23} n m^{-2} ($E > 1$ MeV) is shown in Fig. 10. In addition to phosphorus segregation, several copper-enriched precipitates are evident along the dislocation. Several other substitutional elements such as manganese and silicon have also been observed on dislocations and dislocation loops [30]. In some cases, the distribution of the manganese and silicon were found at different regions of the loop. This effect was attributed to the different accommodations of the undersized manganese and oversized silicon atoms in the stress field associated with the dislocation loop.

The preferential precipitation of copper-enriched precipitates on and the solute segregation to the dislocation will effectively pin these dislocations from movement. These pinned dislocations will act as barriers for glissile dislocations, thereby influencing the mechanical properties. However, the relative importance of the pinned dislocations with their

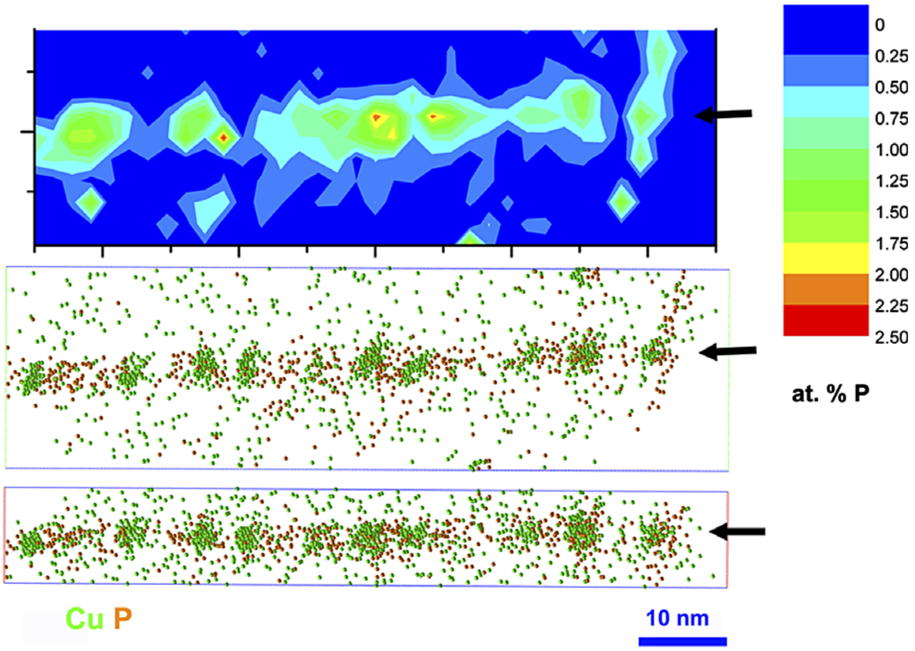

Fig. 10. Example of a two-dimensional concentration map and 2 orthogonal views of an atom map of phosphorus segregation and copper-enriched precipitates on a dislocation in a neutron irradiated weld from the Midland reactor.

associated copper-enriched precipitates versus the matrix copper-enriched precipitates as barriers to the movement of new glissile dislocations remains to be established. The preexisting dislocation density may be an additional factor in determining the mechanical properties after neutron irradiation.

8. Grain boundaries

Grain boundaries are a potential location for the failure of pressure vessel steels by an intergranular fracture mechanism. The susceptibility of grain boundaries to intergranular failure depends on the solute levels at the boundaries, particularly the elements that are responsible for temper embrittlement. Intergranular failure is not common in Western RPV steels.

The atom probe may be used to characterize the level of all the solutes on the grain boundary. In addition, the presence of small precipitates on the grain boundary may be characterized. However, the tens-of-micron grain size of most RPV steels is significantly larger than the typical volume of analysis even for the current generation of wide angle instruments such as the LEAP. Although techniques have been developed to improve the probability of encountering a grain boundary in the analyzable volume of the atom probe specimens by pre-examination in a transmission electron microscope coupled with pulsed electropolishing [6,7], the methods have not been applied to irradiated materials as they require significantly more handling and result in an undesirable oxide film on the surface of the specimen. Moreover, the rapid data acquisition rate of the LEAP can alleviate the problem by improved throughput of specimens. The next generation of wider angle instruments will further improve the situation.

A few studies have been performed on grain boundaries in unirradiated and irradiated RPV steels. Most of the grain boundaries analyzed have been through random encounters in the volume of analysis [31–33]. Field ion microscopy and atom probe analysis revealed that the lath and grain boundaries in A533B, A302B, 15Kh2MFA (VVER440) and 15Kh2NMFA (VVER1000) are decorated with a thin film of molybdenum carbonitride precipitates. The level of phosphorus segregation at lath and grain boundaries in unirradiated steels was found to be in good agreement with the predictions of the McLean model of equilibrium segregation [32,34]. For example in a 15Kh2MFa Cr–Mo–V VVER steel with an abnormally high phosphorus content of 0.058 at.% P, the phosphorus interfacial excess was measured to be $\Gamma_{\mathrm{i}} = 2.8 \times 10^{18}$ atoms m^{-2}. This excess is equivalent to a coverage of ∼13% of a monolayer which is in good agreement with the McLean model prediction of 12% of a monolayer. Neutron irradiation was found to significantly increase the level of phosphorus segregation to lath and grain boundaries. In this same steel, the interfacial excess increased to a maximum of $\Gamma_{\mathrm{i}} = 1.3 \times 10^{19}$ atoms m^{-2} (∼60% of a monolayer) after neutron irradiation to a fluence of 1.15×10^{24} n m^{-2}. The phosphorus coverage was found to increase with both phosphorus content of the alloy and fluence [32]. Other elements including manganese, molybdenum and carbon were also found to be enriched at the boundaries [11].

9. Post irradiation annealing studies

Several studies have indicated that the mechanical properties of the irradiated RPV steel may be recovered, at least in part, by extended (∼168 h) post irradiation annealing of the vessel in the temperature range ∼350 to ∼450 °C [35–44]. For a preexisting nuclear reactor vessel, this upper temperature is the technically achievable temperature limit. If the mechanical properties of the steel are recovered without introducing any other detrimental effects, it should be possible to extend the life of a reactor. Two mechanisms have been proposed for the recovery of the properties; dissolution of the copper-enriched precipitates or coarsening of these precipitates to reduce their number density and effectiveness [45]. The dissolution mechanism essentially returns the alloy to its original unirradiated condition. Consequently, the alloy should re-embrittle at approximately the same rate as during the initial irradiation. The coarsening mechanism should not result in re-embrittlement at the same rate as the solute level in the matrix of the alloy is lower.

The APT results of several post irradiation annealing studies on different steels, including a weld from the Midland reactor [45], a weld from the Babcock and Wilcox Master Integrated Reactor Vessel Surveillance Program [46], 15Kh2MFA steel [47,48] and JRQ weld [49]. The copper levels in the matrix after the stress relief (SR) treatment, neutron irradiation (I), post irradiation annealing (IA), and re-irradiation (IAR) are summarized in Table 1. In all the steels studied, the copper level in the matrix was reduced after neutron irradiation due to the

Table 1
Atom probe tomography results of the copper content (at.%) in the matrix of different steels after the stress relief treatment (SR), irradiation (I), annealing (IA), and re-irradiation (IAR)

Material	Cu after SR	Fluence 10^{23} m^{-2}	Cu after I	PIA	Cu after IA	Fluence 10^{23} m^{-2}	Cu after IAR	Ref.
Midland weld	0.119 ± 0.007	1.1 $E > 1$ MeV	0.06 ± 0.01	168 h at 454 °C	0.05 ± 0.01			[44]
B&W weld	0.14 ± 0.03	3.5 $E > 1$ MeV	0.05 ± 0.01	168 h at 454 °C	0.04 ± 0.02			[45]
Weld 73W	0.12 ± 0.01	1.8 $E > 1$ MeV	0.06 ± 0.01	168 h at 454 °C	0.04 ± 0.01	0.8 $E > 1$ MeV	0.04 ± 0.01	[49]
15Kh2MFA	0.14 nominal	9.7 $E > 0.5$ MeV	0.05 ± 0.02	150 h at 475 °C	0.07 ± 0.03	9.7 $E > 0.5$ MeV	0.05 ± 0.02	[46,47]
JRQ	0.12 ± 0.01	5 $E > 1$ MeV	0.07 ± 0.01	168 h at 460 °C	0.06 ± 0.01			[48]
JRQ	0.12 ± 0.01	0.85 $E > 1$ MeV	n/a	168 h at 460 °C	n/a	0.85 $E > 1$ MeV	0.09 ± 0.01	[48]

formation of the copper-enriched precipitates. Annealing the neutron irradiated material slightly reduced the copper level in the matrix. In the weld from the Midland reactor, some copper-enriched precipitates were observed by field ion microscopy in the matrix after the annealing treatment [45]. In the JRQ steel, coarser copper-enriched precipitates were also observed in the matrix after the annealing treatment [49]. The average size of the copper-enriched precipitates increased from 0.87 to 1.4 nm from the neutron irradiated material to the post irradiation annealed condition.

An atom probe study was performed on a submerged arc weld from the Midland reactor after neutron irradiation to a fluence 1.1×10^{23} m^{-2} at a temperature of 288 °C and post irradiation annealing treatment. In agreement with thermodynamic predictions, this study revealed that thermal annealing of the unirradiated weld for 168 h at 454 °C reduced the copper level in the matrix from 0.119 ± 0.007 to 0.088 ± 0.012 at.% Cu through the formation of copper-enriched precipitates. Similar small reductions from 0.05 ± 0.01 (fluence 3.5×10^{23} m^{-2} at 288 °C) to 0.04 ± 0.02 at.% Cu was also observed in a (0.24 at.% Cu bulk, 0.14 ± 0.03 at.% Cu stress-relieved) weld after the same post irradiation annealing treatment of 168 h at 454 °C. These studies support the coarsening mechanism rather than the dissolution mechanism.

Another APT study of a weld containing 0.14 wt% Cu also revealed the formation of copper-enriched precipitates during the initial irradiation (fluence of 9.7×10^{23} m^{-2} ($E > 0.5$ MeV)), dissolution and growth of these precipitates during the thermal anneal (150 h at 475 °C), but no additional copper-enriched precipitates were detected in the volume analyzed after re-irradiation to an additional fluence of 9.7×10^{23} m^{-2} ($E > 0.5$ MeV) [47,48].

An APT study was also performed on a submerged arc weld (73 W) containing 0.12 at.% Cu in the matrix after the stress anneal. This study was initially performed on a traditional 3DAP [50] and was later repeated on a local electrode atom probe. The significantly larger sampling capabilities of the local electrode atom probe enabled a more complete characterization of the low number density precipitates formed during the thermal annealing treatments. This study revealed the formation of Cu-, Ni-, Mn-, Si-enriched precipitates ($l_g = 0.9$ nm, $N_v = 6 \times 10^{23}$ m^{-3}) during the initial irradiation to a fluence of 1.8×10^{23} m^{-2} ($E > 1$ MeV), and dissolution and growth of these precipitates ($l_g = 1.3$ nm, $N_v = 5 \times 10^{22}$ m^{-3}) during the thermal anneal for 168 h at 454 °C. The matrix copper level decreased slightly from 0.06 to 0.04 at.% Cu during the annealing treatment. Some additional smaller precipitates ($l_g = 0.6$ nm) were formed after re-irradiation to an additional fluence of 6.3×10^{23} m^{-2} ($E > 1$ MeV), IAR, as well as the coarse precipitates ($l_g = 1.5$ nm). No depletion in the 0.04 at.% Cu level in the matrix was detected after this re-irradiation. However, the depletion may have been less than the error in the measurements. After an additional annealing treatment of 168 h at 454 °C, IARA, the finer precipitates were no longer present in the matrix. Atom maps of this precipitation and dissolution sequence are shown in Fig. 11. The coarse precipitates were found to be preferentially located on the dislocations.

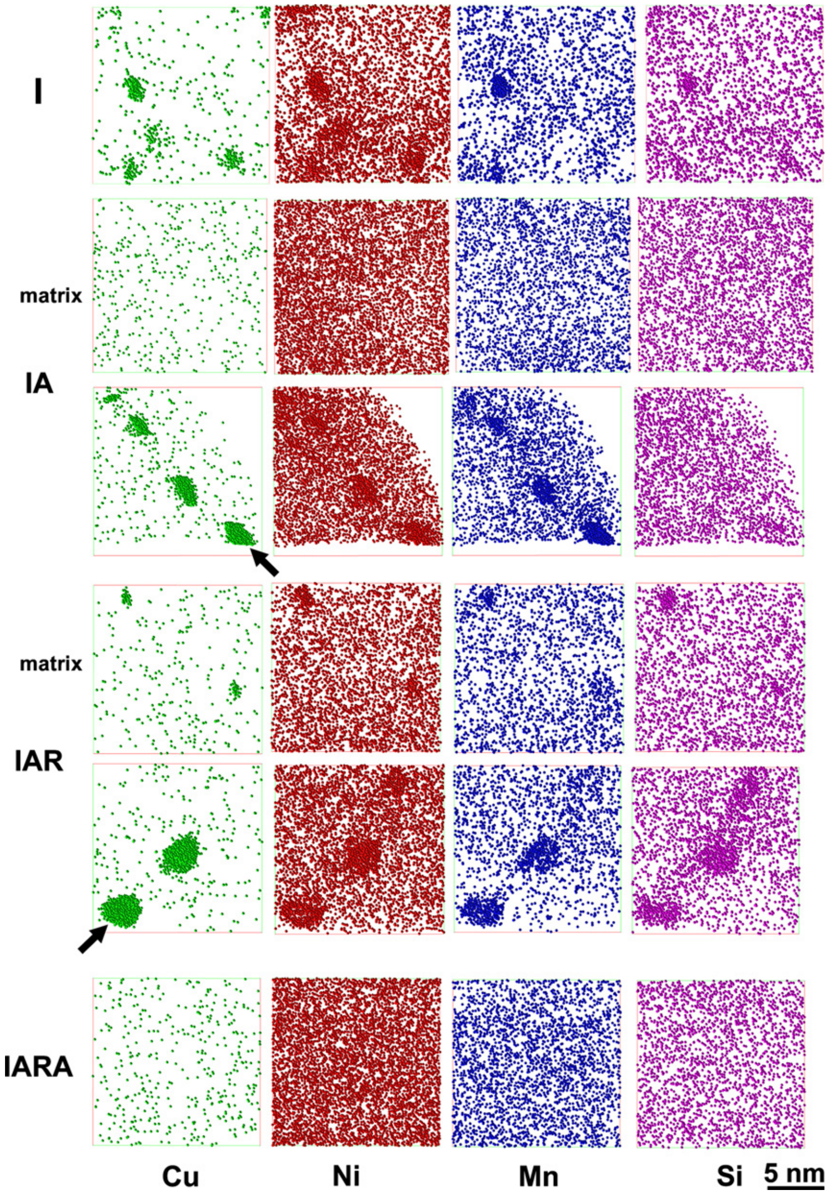

Fig. 11. Atom maps of submerged arc weld (73 W) revealed the formation of Cu-, Ni-, Mn-, Si-enriched precipitates during irradiation to a fluence of 1.8×10^{23} m^{-2} ($E > 1$ MeV), I, dissolution and growth of these precipitates during a thermal anneal for 168 h at 454 °C, IA, the formation of some additional precipitates after re-irradiation to an additional fluence of 6.3×10^{23} m^{-2} ($E > 1$ MeV), IAR, and their dissolution after another thermal anneal for 168 h at 454 °Cl, IARA. The arrows indicate dislocations.

10. Long term thermal aging

Thermodynamics predict that there is a potential for copper precipitation if the level in the alloy is above the copper supersaturation limit at the operating temperature of nuclear reactors (typically 280 °C). However, the predicted diffusion rates of substitutional solutes at these low temperatures are negligible. A few atom probe studies have been performed to determine whether any precipitation occurs during long term thermal aging [51,52]. In these experiments, the thermal aging specimen boxes were attached to the service support structure on top of the reactor vessel head [Oconee Nuclear Station, Unit 3 (ONS3)] and are located under the head insulation. In this study, a SA-533 grade B class 1 plate B (HSST-02, A1195-1), SA-508 class 2 forging A (ANK 191) and a submerged arc weld

Table 2
Alloy compositions and mechanical property data for long term thermally aged A533B plate, SA-508 forging and submerged arc weld materials [53]

Element	Plate B		Forging A		Weld B	
	wt%	at.%	wt%	at.%	wt%	at.%
Alloy compositions						
Copper	0.17	0.15	0.02	0.02	0.30	0.26
Nickel	0.64	0.60	0.76	0.72	0.58	0.55
Manganese	1.39	1.40	0.72	0.72	1.63	1.64
Silicon	0.21	0.41	0.21	0.41	0.61	1.20
Molybdenum	0.50	0.29	0.62	0.36	0.39	0.22
Chromium	–	–	0.34	0.36	0.10	0.10
Carbon	0.23	1.06	0.24	1.11	0.08	0.37
Phosphorus	0.013	0.023	0.014	0.025	0.017	0.03
Mechanical properties, DBTT, °C and USE, J [52]						
	41 J	USE	41 J	USE	41 J	USE
Unaged	1	130	−37	177	−2	85
93 000 h	7	6120				
103 000 h			−32	180	−7	93
209 000 h	6	5134	−23	173	−3	76

Courtesy Gunawardane and Hall of AREVA.

Table 3
Compositions of the matrix in the forging after thermal annealing for 209 000 h at 260 °C

at.%	Alloy	Unaged	103k	209k
Cu	0.02	0.03 ± 0.01	0.03 ± 0.02	0.03 ± 0.01
Ni	0.72	0.72 ± 0.01	0.63 ± 0.10	0.73 ± 0.01
Mn	0.72	0.48 ± 0.06	0.53 ± 0.09	0.37 ± 0.01
Si	0.41	0.50 ± 0.06	0.44 ± 0.08	0.50 ± 0.01
Mo	0.36	0.12 ± 0.01	0.08 ± 0.01	0.13 ± 0.01
Cr	0.36	0.15 ± 0.03	0.20 ± 0.05	0.20 ± 0.01
C	1.11	0.004 ± 0.004	–	0.01 ± 0.01
P	0.025	0.02 ± 0.01	0.003 ± 0.003	0.02 ± 0.01

Material courtesy Gunawardane and Hall of AREVA.

B–Mn–Mo–Ni weld wire/Linde 80 flux (WF-209-1) were placed on the reactor vessel heads before startup and were removed from ONS-3 after an exposure time of either 93 000 or 103 000 and 209 000 h ($\sim$24 years) at a temperature of $\sim$260 °C [53]. The exact exposure time for each set of materials was difficult to determine because of the time allowance for reactor heatup, cooldown and hot standby. To account for these transitions, the stated aging times reflect a 10% increase of the actual effective full power times when the surveillance materials were removed. Because of its location, the surveillance material was considered to have negligible neutron fluence exposure which was experimentally verified. The bulk compositions of these alloys and the change in mechanical properties during extended aging treatments are given in Table 2 [53]. Small changes in the impact properties were observed, but were generally within the 95% confidence bounds for typical Charpy data [53]. Upper-shelf energy showed small variations. Master curve T_0 testing in the transition region showed little change in the forging and plate and a small improvement in the weld [53].

The matrix compositions of the SA-508 forging after the thermal aging treatments as determined by APT are listed in Table 3. No significant changes were evident after the extended aging treatments. No fine precipitates were observed in the SA-508 forging or SA-533 plate after aging for 209 000 h. Atom probe analysis of the matrix revealed that the copper level in the forging was 0.03 at.% Cu and within the experimental scatter of the alloy composition. The low copper content of the forging is below the level at which Cu-enriched precipitates are typically observed.

A few relatively coarse rod-shaped precipitates were observed in the weld that was thermally aged for 103 000 h at 260 °C, as shown in Fig. 12. The Guinier radii of these precipitates were estimated to be between 2 and 5 nm. A concentration profile through this precipitate is shown in Fig. 13. Some enrichment of manganese in the precipitate and the nickel and manganese enrichments at the precipitate–matrix interface are evident. The relatively coarse nature of these precipitates indicated that they likely formed during the high temperature stress relief treatment rather than during the

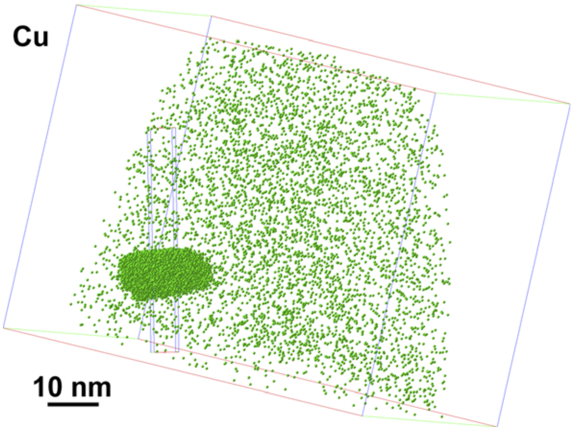

Fig. 12. A copper atom map containing a copper-enriched precipitate in the submerged arc weld after long term thermal aging for 103 000 h at 260 °C. The radius of gyration of this precipitate was 5 nm. Material courtesy Gunawardane and Hall of AREVA [53].

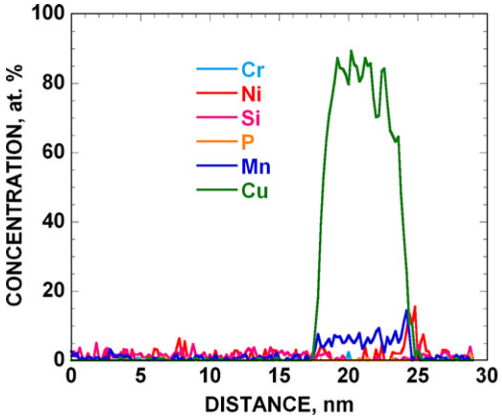

Fig. 13. A 4 × 4 nm cross-section concentration profile through the central region of the precipitate shown in Fig. 12. Note the enrichment of manganese in the precipitate and the nickel and manganese enrichments at the precipitate–matrix interface. Material courtesy Gunawardane and Hall of AREVA [53].

extended aging treatment and was accompanied by the reduction in the matrix copper level from 0.3 to 0.2 at.%. However, the possibility of some coarsening during the aging treatment cannot be excluded. In contrast, a low number density, $\sim 10^{22}\ \mathrm{m}^{-3}$, of copper- and manganese-enriched precipitates was observed in the weld after aging for 209 000 h, as shown in Fig. 14. This number density

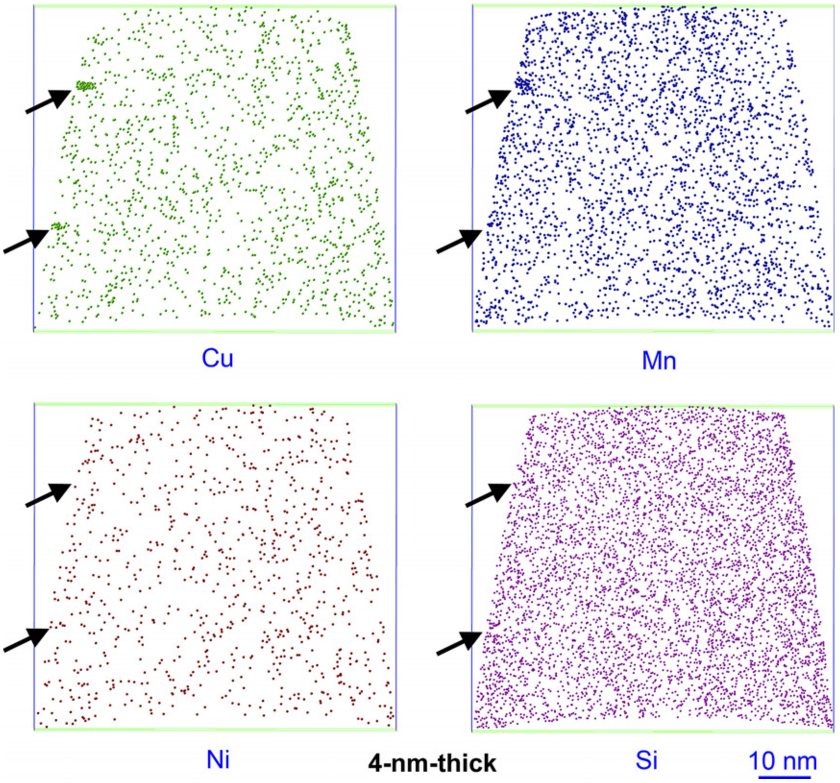

Fig. 14. A 4-nm-thick atom map containing ultrafine copper- and manganese-enriched precipitates in the submerged arc weld after long term thermal aging for 209 000 h at 260 °C. Material courtesy Gunawardane and Hall of AREVA [53].

is significantly lower than the typical number density observed in neutron irradiated welds. The average Guinier radius of these precipitates was estimated to be 1.0 ± 0.2 nm. A small decrease in the matrix copper content to 0.16 ± 0.01 at.% Cu was also measured. This matrix level is higher than the copper level in the plate indicating that precipitates are not likely to form in the plate under these aging conditions. The absence of ultra fine precipitates after the 103 000 h aging treatment could be due to a long incubation period or their size was too small to be resolved above the random fluctuations. Therefore, these results indicate that it is possible to form a low number density of copper-enriched precipitates by thermal aging at the reactor temperature in high copper welds. However their contribution to embrittlement is negligible. The thermal aging results indicate that neutron radiation enhances the formation of the copper-enriched precipitates.

11. Conclusions

Atom probe tomography has proved to be an invaluable tool for the characterization of the microstructure of neutron irradiated pressure vessel steels. Atom probe tomography has revealed that:

- The post weld stress relief treatment reduces the matrix copper content in high copper alloys thereby making these alloys less susceptible to embrittlement.
- ~2-nm-diameter copper-, nickel-, manganese- and silicon-enriched precipitates formed during neutron irradiation in copper containing RPV steels.
- The copper-enriched precipitates coarsened during post irradiation heat treatments and a second finer distribution formed during re-irradiation.
- Solute segregated to and precipitated on dislocations and grain boundaries.
- ~2-nm-diameter nickel-, silicon- and manganese-enriched clusters formed in neutron irradiated high nickel, low copper and copper free alloys.
- Fine copper-enriched precipitates formed during long term thermal exposure at the reactor temperature.

Acknowledgements

This research was conducted at the Oak Ridge National Laboratory SHaRE User Facility, which is sponsored by the Office of Basic Energy Sciences, Division of Scientific User Facilities, US Department of Energy, under Contract DE-AC05-00OR22725 with UT-Battelle, LLC. This research was also supported by the Office of Nuclear Regulatory Research, US Nuclear Regulatory Commission under inter-agency agreement DOE 1886-N695-3W with the US Department of Energy. The authors thank H. Gunawardane and J.B. Hall of AREVA for providing the long term thermally aged steels and G.R. Odette of the University of California-Santa Barbara and R.K. Nanstad, R.E. Stoller and M.A. Sokolov of ORNL for their assistance and helpful discussions.

References

[1] S.S. Brenner, R. Wagner, J.A. Spitznagel, Metall. Trans A 9 (1978) 1761.
[2] R.E. Lott, S.S. Brenner, M.K. Miller, A. Wolfenden, Proc. Am. Nucl. Soc., Trans. 38 (1981) 303.
[3] M.K. Miller, S.S. Brenner, Res. Mech. 10 (1984) 161.
[4] M.K. Miller, G.D.W. Smith, Atom Probe Microanalysis: Principles and Applications to Materials Problems, Materials Research Society, Pittsburgh, PA, 1989.
[5] M.K. Miller, M.G. Hetherington, M.G. Burke, Metall. Trans. A 20 (1989) 2651.
[6] M.K. Miller, A. Cerezo, M.G. Hetherington, G.D.W. SmithMonographs on the Physics and Chemistry of Materials, vol. 52, Oxford University, Oxford, 1996.
[7] M.K. Miller, Atom Probe Tomography, Kluwar Academic/Plenum Publishing, New York, NY, 2000.
[8] M.K. Miller, Mater. Charact. 44 (2000) 11.
[9] M.K. Miller, P. Pareige, M.G. Burke, Mater. Charact. 44 (2000) 235.
[10] P. Auger, P. Pareige, S. Welzel, J.-C. Van Duysen, J. Nucl. Mater. 280 (2000) 331.
[11] M.K. Miller, P. Pareige, in: G.E. Lucas, L. Snead, M.A. KirkJr., R.G. Elliman (Eds.), Proceedings of the MRS 2000 Fall Meeting, Symposium R: Microstructural Processes in Irradiated Materials, Boston, MA, November, 27–30, 2000, vol. 650, Materials Research Society, Pittsburgh, PA, 2001, p. R6.1.1.
[12] J.M. Hyde, C.A. English, in: G.E. Lucas, L. Snead, M.A. KirkJr., R.G. Elliman (Eds.), Proceedings of the MRS 2000 Fall Meeting, Symposium R: Microstructural Processes in Irradiated Materials, Boston, MA, November, 27–30, 2000, vol. 650, Materials Research Society, Pittsburgh, PA, 2001, p. R6.6.1.
[13] M.K. Miller, in: A. Gonis, P.E.A. Turchi, A.J. Ardell (Eds.), Proceedings of the MRS 1999 Fall Meeting, Symposium E: Nucleation and Growth Process in Materials, Boston, MA, November, 29–December, 2, 1999, vol. 580, Materials Research Society, Warrendale, PA, 2000, p. 35.
[14] M.K. Miller, B.D. Wirth, G.R. Odette, Mater. Sci. Eng. A. 353 (2003) 133.
[15] O.C. Hellman, J.A. Vandenbroucke, J. Rüsing, D. Isheim, D.N. Seidman, Microsc. Microanal. 6 (2000) 437.

[16] M.K. Miller, S.S. Babu, M.A. Sokolov, R.K. Nanstad, S.K. Iskander, Mater. Sci. Eng. A 327 (2002) 76.

[17] M. Perez, F. Perrard, V. Massardier, X. Kleber, A. Deschamps, H. De Monestrol, P. Pareige, G. Covarel, Philos. Mag. 85 (2005) 2197.

[18] M.K. Miller, K.F. Russell, J. Nucl. Mater. 250 (1997) 223.

[19] M.K. Miller, M.A. Sokolov, R.K. Nanstad, S.K. Iskander, in: Proceedings of the 10th International Conference on Environmental Degradation of Materials in Nuclear Power Systems-Water Reactors, Lake Tahoe, NV, August, 5–9, 2001, pub. NACE, 2002, CD.

[20] M.K. Miller, S.S. Babu, M.A. Sokolov, R.K. Nanstad, S.K. Iskander, Mater. Sci. Eng. A 327 (2002) 76.

[21] M.K. Miller, K.F. Russell, M.A. Sokolov, R.K. Nanstad, J. Nucl. Mater. 320 (2003) 177.

[22] M.K. Miller, K.F. Russell, M.A. Sokolov, R.K. Nanstad, Philos. Mag. 85 (2005) 401.

[23] M.K. Miller, K.F. Russell, M.A. Sokolov, R.K. Nanstad, J. Nucl. Mater. 361 (2007) 248.

[24] P.J. Pareige, M.K. Miller, Appl. Surf. Sci. 94&95 (1996) 370.

[25] M.K. Miller, R.K. Nanstad, M.A. Sokolov, K.F. Russell, J. Nucl. Mater. 351 (2006) 187.

[26] G.R. Odette, T. Yamamoto, B.D. Wirth, in: N.M. Ghoniem (Ed.), Proceedings of the Second International Conference on Multiscale Materials Modeling, University of California, 2004, p. 355.

[27] M.K. Miller, TMS Lett. 1 (2004) 19.

[28] M.K. Miller, Microsc. Res. Techniq. 69 (2006) 359.

[29] M.K. Miller, J. Mater. Sci. 41 (2006) 7808.

[30] M.K. Miller, K.F. Russell, J. Kocik, E. Keilova, J. Nucl. Mater. 282 (2000) 83.

[31] M.K. Miller, R. Jayaram, K.F. Russell, J. Nucl. Mater. 225 (1995) 215.

[32] M.K. Miller, K.F. Russell, Appl. Surf. Sci. 94&95 (1996) 378.

[33] M.K. Miller, R. Jayaram, K.F. Russell, Mater. Res. Soc. Symp. Proc. 373 (1995) 113.

[34] D. McLean, Grain Boundaries in Metals, Oxford University, London, 1957, p. 116.

[35] J.R. Hawthorne, in: Conference on Steels for Reactor Pressure Circuits, Special Report 69, Iron and Steel Institute for the British Nuclear Energy, 1961, p. 343.

[36] J.R. Hawthorne, H.E. Watson, F.L. Loss, in: J.A. Sprague, D. Kramer (Eds.), Effects of Radiation on Structural Materials, ASTM STP 683, American Society for Testing and Materials, Philadelphia, PA, 1978, p. 278.

[37] J.R. Hawthorne, H.E. Watson, F.L. Loss, in: D. Kramer, H.R. Prager, J.S. Perrin (Eds.), Proceedings of the 10th Conference on Effects of Radiation in Materials, ASTM STP 725, American Society for Testing and Materials, Philadelphia, PA, 1981, p. 63.

[38] R.G. Lott, T.R. Mager, R.P. Shogan, S.E. Yanichko, in: L.E. Steele (Ed.), Radiation Embrittlement of Nuclear Reactor Pressure Vessel Steels, An International Review, ASTM STP 909, vol. 2, American Society for Testing and Materials, Philadelphia, PA, 1986, p. 242.

[39] J.R. Hawthorne, in: F.A. Garner, C.H. Hanager, N. Igata (Eds.), Thirteenth International Symposium on Influence of Radiation on Materials Properties Part II, ASTM STP 956, American Society for Testing and Materials, Philadelphia, PA, 1987, p. 461.

[40] J.R. Hawthorne, A.L. Hiser, in: D. Cubicciotti, E.P. Simonen, R.E. Gold (Eds.), Proceedings of the Fifth International Symposium on Environmental Degradation of Materials in Nuclear Power Systems-Water Reactors, Monterey 1991, American Nuclear Society, La Grange Park, IL, 1992, p. 671.

[41] G.R. Odette, G.E. Lucas, Radiat. Eff. Def. 144 (1–4) (1998) 189.

[42] E. Mader, G.E. Lucas, G.R. Odette, in: Effects of Radiation on Materials: 15th International Symposium, ASTM STP 1125, 1992, p. 151.

[43] M.A. Sokolov, S. Spooner, G.R. Odette, B.D. Wirth, G.E. Lucas, in: Effects of Radiation on Materials: 18th International Symposium, ASTM STP 1325, 1999, p. 333.

[44] E.E. Eason, J.E. Wright, G.R. Odette, Nucl. Eng. Des. 179 (1998) 257.

[45] M.K. Miller, K.F. Russell, J. Nucl. Mater. 250 (1997) 223.

[46] P. Pareige, R.E. Stoller, K.F. Russell, M.K. Miller, J. Nucl. Mater. 249 (1997) 165.

[47] P. Pareige, B. Radiguet, A. Suvorov, M. Kozodaev, E. Krasidov, O. Zabusov, J.P. Massoud, Surf. Interf. Anal. 36 (2004) 581.

[48] P. Pareige, B. Radiguet, R. Ummeich-Brangier, A. Barbu, O. Zabusov, M. Kozodaev, Philos. Mag. 85 (2005) 429.

[49] M.K. Miller, R.K. Nanstad, M.A. Sokolov, K.F. Russell, J. Nucl. Mater. 351 (2006) 216.

[50] M.K. Miller, K.F. Russell, P. Pareige, in: G.E. Lucas, L. Snead, M.A. KirkJr., R.G. Elliman (Eds.), Proceedings of the MRS 2000 Fall Meeting, Symposium R: Microstructural Processes in Irradiated Materials, Boston, MA, November, 27–30, 2000, vol. 650, Materials Research Society, Pittsburgh, PA, 2001, p. R3.15.1.

[51] P. Pareige, K.F. Russell, R.E. Stoller, M.K. Miller, J, Nucl. Mater. 250 (1997) 176.

[52] P.J. Pareige, M.K. Miller, R.E. Stoller, in: Proceedings of the International Workshop on Aged and Decommissioned Materials Collection and Testing for Structural Integrity Purposes, vol. 17, 1995, p. 117.

[53] H.P. Gunawardane, J.B. Hall, S.T. Rosinski, J. ASTM Int. 3 (2) (2006), Paper ID JAI12430.